

Optical transitions in Mn^{3+} -doped garnets

S. Kück,* S. Hartung, S. Hurling, K. Petermann, and G. Huber

Institut für Laser-Physik, Universität Hamburg, Jungiusstraße 9a, 20355 Hamburg, Germany

(Received 22 July 1997)

The optical spectra of Mn^{3+} -doped garnet crystals reveal a large Jahn-Teller stabilization energy of about 1900 cm^{-1} for the 5E ground state, and smaller Jahn-Teller stabilization energies for the excited states, i.e., $\approx 325 \text{ cm}^{-1}$ for the 5T_2 , and $\approx 180 \text{ cm}^{-1}$ for the 1T_2 level. The absorption spectra are dominated by the spin-allowed ${}^5E \rightarrow {}^5T_2$ transition. At low temperatures, the emission occurs from the 1T_2 level to the Jahn-Teller-split ground state and the 3T_1 intermediate level. With increasing temperature the 5T_2 level becomes thermally populated and the emission spectrum is dominated by the spin-allowed ${}^5T_2 \rightarrow {}^5E$ transition. The emission lifetime is nearly independent of the detection wavelength, but strongly dependent of the temperature and the host lattice. At 12 K the lifetime is $\approx 6 \text{ ms}$ for all crystals, while at room temperature it is between 1.1 ms for $\text{Mn}^{3+}:\text{Y}_3\text{Al}_5\text{O}_{12}$ and $< 0.5 \mu\text{s}$ for $\text{Mn}^{3+}:\text{Gd}_3\text{Sc}_2\text{Ga}_3\text{O}_{12}$. The radiative lifetimes of the 1T_2 and 5T_2 levels were determined to be about 6 ms and 16 μs , respectively. Both the radiative and the nonradiative rate are temperature dependent due to the coupling of odd-parity and totally-symmetric phonons, and the thermalization of the 5T_2 level. The nonradiative decay is more pronounced for lower crystal-field strengths, because of the smaller ${}^5T_2 - {}^3T_1$ energy gap and the higher population of the 5T_2 level. Excited-state absorption transitions arising from the energetically lower 1T_2 in higher lying singlet levels cover the entire spectral range of the emission; therefore laser oscillation at room temperature is unlikely in Mn^{3+} -doped garnets. [S0163-1829(98)06204-3]

I. INTRODUCTION

The Jahn-Teller effect¹ can strongly influence the optical spectra of transition-metal-ion-doped materials; see, e.g., Cr^{2+} -doped silver halides,²⁻⁴ Cr^{2+} -doped II-VI semiconductors,⁵ and Ti^{3+} -doped sapphire.⁶⁻⁸ The absorption spectra of the Mn^{3+} ion in octahedral coordination reveal a strong Jahn-Teller distortion in the 5E ground state.^{6,9,10} Mn^{3+} emission at room temperature was observed in $\text{Y}_3\text{Al}_5\text{O}_{12}$,¹¹ however, until now the influence of the Jahn-Teller distortion and the thermalization of different energy levels on the emission characteristic was not investigated. One aim of this work was to develop a model describing the observed optical transitions.

Most transitions of $3d$ ions in crystals exhibit a strong electron-phonon coupling. As a result, the observed transitions between the different energy levels are broadened. The coupling of odd-parity phonons yields a temperature-dependent radiative rate,¹² while the nonradiative rate increases with temperature due to multiphonon processes.¹³ In this paper temperature-dependent lifetime and emission intensity measurements are presented and analyzed in detail. A model for the description of the observed temperature dependencies is developed.

Since the development of the $\text{Ti}^{3+}:\text{Al}_2\text{O}_3$ laser,¹⁴⁻¹⁷ with its outstanding tuning range of 670–1100 nm and its high efficiency, much research has been performed on new tunable solid-state lasers for shorter wavelength regions, e.g., $\text{Ti}^{3+}:\text{YAlO}_3$ (Ref. 18) and $\text{V}^{4+}:\text{Al}_2\text{O}_3$.¹⁹ None of them has been successful yet, mostly because of strong excited-state absorption at the pump or laser wavelength. Moreover, tunable solid-state lasers in the spectral region between 600 and 700 nm are interesting for a variety of applications, e.g., display technology, medicine, and spectroscopy. The Mn^{3+}

ion seems to be an interesting candidate for an active laser center for this spectral region, because its emission covers the entire wavelength region between 550 and 1300 nm.

The crystal-field dependence of the Mn^{3+} energy levels is shown in the Tanabe-Sugano diagram for a d^4 electron configuration;²⁰ see Fig. 1. The Mn^{3+} energy-level diagram

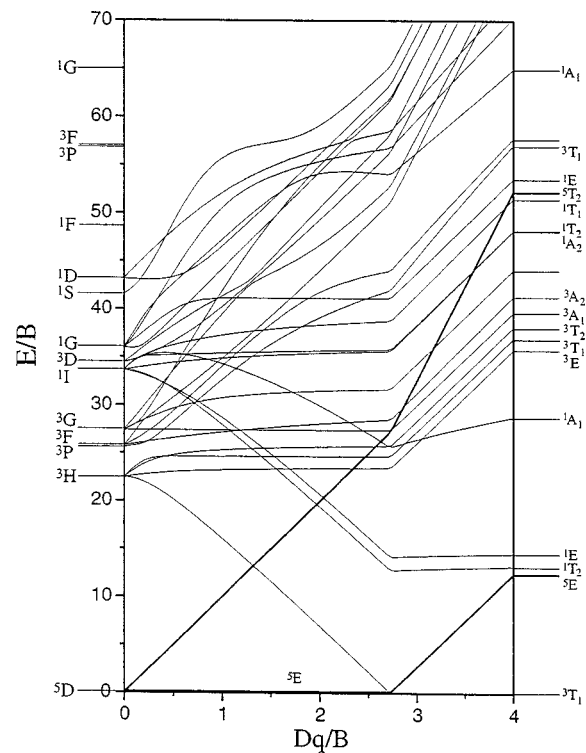


FIG. 1. Tanabe-Sugano diagram for a d^4 -electron configuration in octahedral symmetry.

TABLE I. Data of the investigated Mn³⁺-doped garnets.

Crystal		GSGG	YSGG	GGG	YGG	YAG
{C} site		Gd	Y	Gd	Y	Y
[A] site		Sc, Ga	Sc, Ga	Ga	Ga	Al
(D) site		Ga	Ga	Ga	Ga	Al
Lattice constant	(pm)	1259	1243	1238	1228	1200
Melting temperature	(°C)	1850	1780	1730	1790	1930
Density	(g/cm ³)	6.44	5.26	7.02	5.73	4.55
Growth atmosphere		N ₂ +1%O ₂	N ₂			
Doping level	(at. %)	0.05	0.05	0.2	0.4	0.4
Mn distribution coefficient			0.124		0.073	

is similar to that of the Cr²⁺ ion (although the coordination is different), which exhibits efficient laser oscillation in II-IV semiconductors on the ⁵E→⁵T₂ transition.²¹ Although for a *d*⁴-electron system a large number of energy levels exists, only two of them are quintet states, i.e., the ⁵E ground state and the ⁵T₂ excited state. Therefore, excited-state absorption transitions from the ⁵T₂ into higher-lying levels are expected to cover a broad wavelength range, but all of these transitions are spin-forbidden; i.e., the excited-state absorption cross section is expected to be much smaller than the emission cross section of the ⁵T₂→⁵E transition. However, in this paper it will be shown that excited-state transitions from other metastable levels prevent laser action in Mn³⁺-doped garnets.

II. CRYSTAL GROWTH

All crystals under investigation were Mn-doped garnets, that are Y₃Al₂O₁₂ (YAG), Y₃Ga₅O₁₂ (YGG), Gd₃Ga₅O₁₂ (GGG), Y₃Sc₂Ga₃O₁₂ (YSGG), and Gd₃Sc₂Ga₃O₁₂ (GSGG). Garnets are cubic crystals with space group *Ia3d* (*O*_h¹⁰ in Schoenflies notation).²² The stoichiometric formula is {C}₃[A]₂(D)₃O₁₂, where C, A, and D denote lattice sites with dodecahedral, octahedral, and tetrahedral coordinations, respectively, and with site symmetries *D*₂, *C*_{3i}, and *S*₄, respectively. The crystals were grown by the Czochralski method using an iridium crucible and rf heating. Some properties of the host crystals are listed in Table I.

In general, manganese ions are found in different valence states from divalent to septavalent. Therefore, manganese ions with different valence states are likely incorporated in the crystals, although all constituent ions in the garnet host crystals are trivalent. In order to stabilize the trivalent state, an inert growth atmosphere seems reasonable. However, for the gallium garnets (YGG, GGG, YSGG, and GSGG) a slightly oxidizing atmosphere is necessary in order to prevent Ga-suboxide evaporation from the melt and to achieve a reasonable crystal quality. As a result, Mn⁴⁺ at octahedral sites was also found in the spectra of these crystals. Attempts to anneal these crystals in a reducing atmosphere—in order to achieve a valence change—failed, because of surface damage of the crystals. The surface damage is most probably caused by reduction of gallium ions to metallic gallium. For Mn:YAG and Mn:YSGG, traces of Mn²⁺ were also found spectroscopically. The Mn³⁺ ions occupy the octahedrally coordinated lattice site. No hints on dodecahedrally or tetra-

hedrally coordinated Mn³⁺ were found. The growth conditions for the different crystals are also listed in Table I.

The total manganese concentrations in the crystals were determined for YSGG and YGG with atomic emission spectroscopy. Therefore, the manganese distribution coefficients given in Table I have to be considered as upper limits for the Mn³⁺ ion. The observed distribution coefficient is low, although the ionic radii of manganese and the constituent lattice ions are rather similar;²³ see Table II.

III. SPECTROSCOPIC METHODS AND EXPERIMENTAL SETUPS

The room-temperature absorption spectra were measured with a CARY 2400 spectrophotometer. The fluorescence measurements were performed under argon-ion laser excitation at 514.5 nm. The emission was detected with a photomultiplier with S1 characteristic or a cooled InSb-detector, which were placed behind a 0.5-m spectrometer. The spectral resolutions were 1.6 nm between 500 and 1000 nm, and 3.2 nm between 1000 and 1500 nm. Appropriate optical filters were used to block scatter light of the excitation beam and to avoid second-order effects. For the low-temperature measurements, the crystal was placed in a closed-cycle helium cryostat. In this case the resolutions were 0.8 nm (500–1000 nm), 1 nm (1000–1500 nm; YAG and GGG), and 1.6 nm (1000–1500 nm; YGG, YSGG, and GSGG). The temperature-dependent fluorescence intensity measurements were carried out with the same setup, but with fixed detection wavelengths around 620 and 1120 nm and resolutions of 1.6 and 4 nm, respectively.

The temperature-dependent lifetime measurements were

TABLE II. Ionic radii of the constituent and substituting ions (Ref. 23).

Site	Cation	Size (pm)	Mn ²⁺ (pm)	Mn ³⁺ (pm)	Mn ⁴⁺ (pm)
C	Y ³⁺	102	93		
	Gd ³⁺	106			
A	Al ³⁺	53			
	Ga ³⁺	62	83	65	54
	Sc ³⁺	75			
D	Al ³⁺	39			
	Ga ³⁺	47			

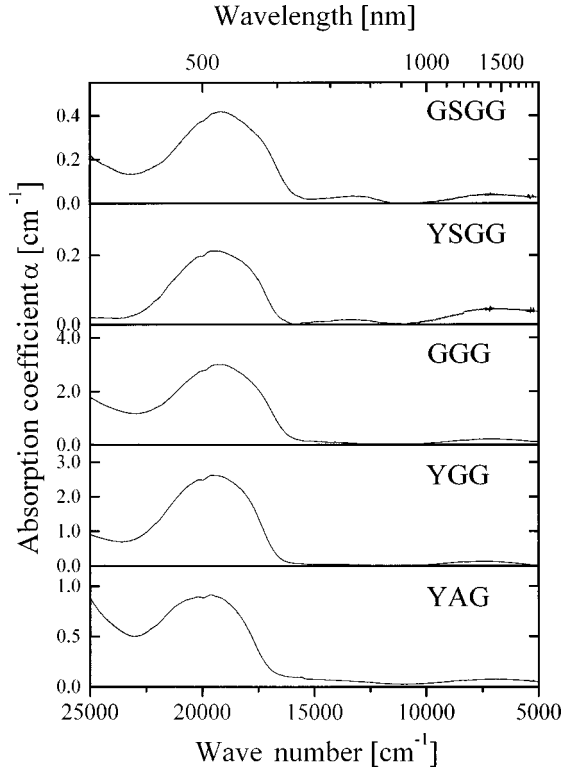


FIG. 2. Room-temperature absorption spectra of Mn³⁺-doped garnets.

carried out under excitation with a Q -switched, frequency-doubled Nd:YAG laser operating at 532 nm with a pulse length of 10 ns. The crystals were placed again in a closed-cycle helium cryostat.

The excited-state absorption measurements were performed at room temperature with a pump-and-probe technique in the continuous-wave regime. The double-modulation technique with two lock-in amplifiers was used, described in detail, e.g., in Refs. 24 and 25. Both the difference in the transmitted intensities in the pumped and unpumped case ($I_p - I_u$) as well as the transmitted intensity

($I \approx I_p \approx I_u$) through the crystal were measured simultaneously. It can be shown that the following equation holds:²⁵

$$\frac{I_p(\lambda) - I_u(\lambda)}{I_p(\lambda)} \propto \sigma_{\text{GSA}}(\lambda) + \sigma_{\text{SE}}(\lambda) - \sigma_{\text{ESA}}(\lambda). \quad (1)$$

Here, σ_{GSA} , σ_{SE} , and σ_{ESA} are the ground-state absorption, stimulated emission, and excited-state absorption cross section, respectively. Pump-and-probe beams were provided by an argon-ion laser operating at 514.5 nm, and a broadband tungsten lamp, respectively. The transmitted intensities were measured with a Si detector or a cooled InSb detector, which was placed behind a 0.5-m spectrometer. The spectral resolution was 3.2 nm for the entire spectral range between 500 and 2000 nm.

IV. RESULTS

The room-temperature absorption spectra are shown in Fig. 2. They are dominated by a strong absorption band with a maximum around 510 nm, and a bandwidth of about 4000 cm⁻¹. A weaker band is also clearly observed in the infrared spectral range with a maximum between 1300 and 1400 nm. In Table III the data of these absorption bands are summarized. Furthermore, a small band around 750 nm is observed in some of the crystals. The strength of this band is strongly dependent on the treatment of the crystal, and is not correlated with the absorption of the other bands, as can be seen for Mn:YSGG in Fig. 3. Therefore this transition—probably a charge-transfer transition based on a photochromatic effect—is not further considered for developing the Mn model. All spectra exhibit a characteristic feature on the short-wavelength side of the 500-nm absorption band; see Fig. 4 for the case of Mn:YAG.

The room-temperature emission spectra are shown in Fig. 5, and the significant data are listed in Table IV. The spectra are dominated by two bands with maxima around 625 (band 1) and around 800 nm (band 2). For Mn³⁺:YAG, a structured emission band around 1100 nm is also observed, which

TABLE III. Data of room temperature absorption, corrected for the background absorption. $\lambda(E)$ is the wavelength (wave number) of the absorption maximum, Γ is the bandwidth, and α (σ) the absorption coefficient (absorption cross section). The index VIS(IR) indicates the values for the ${}^5E \rightarrow {}^5T_2$ (${}^5E \rightarrow {}^5E$) transition. $\Delta E_{\text{JT}}({}^5E)$ is the Jahn-Teller stabilization energy of the 5E level.

Crystal		GSGG	YSGG	GGG	YGG	YAG
λ_{VIS}	(nm)	524	515	521	517	510
E_{VIS}	(cm ⁻¹)	19 084	19 417	19 212	19 361	19 608
Γ_{VIS}	(cm ⁻¹)	4103	4374	4161	4130	3960
α_{VIS}	(cm ⁻¹)	0.36	0.21	2.17	4.02	2.17
σ_{VIS}	(10 ⁻²⁰ cm ²)		4.5		16.6	
λ_{IR}	(nm)	1361	1242	1372	1326	1389
E_{IR}	(cm ⁻¹)	7350	8054	7290	7540	7200
Γ_{IR}	(cm ⁻¹)	3156	3207	3572	3760	3873
$\Gamma_{\text{IR}}/E_{\text{IR}}^{1/2}$	(cm ^{-1/2})	36.8	35.7	41.8	43.3	45.6
α_{IR}	(cm ⁻¹)	0.04	0.04	0.22	0.34	0.23
σ_{IR}	(10 ⁻²⁰ cm ²)		0.74		1.31	
$\alpha_{\text{VIS}}/\alpha_{\text{IR}}$		7.3	6.1	11.5	12.7	9.6
$\Delta E_{\text{JT}}({}^5E)$	(cm ⁻¹)	1838	2014	1823	1885	1800

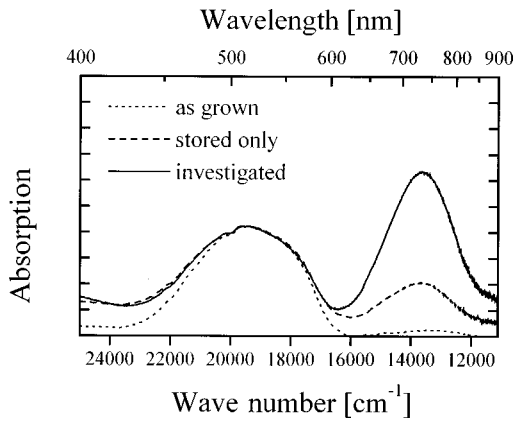


FIG. 3. Influence of the crystal treatment on the absorption spectrum of Mn: YSGG: (1) After growth. (2) Part of the crystal stored under ambient light, after six months. (3) A different part of the crystal, spectroscopically investigated, after six months.

is very weak for Mn^{3+} :YGG and not observed in the other crystals.

The 12-K emission spectra are shown in Fig. 6. The data are summarized in Tables V and VI. The 12-K spectra also consist of two bands. However, their energetic positions are significantly shifted into the infrared spectral region. The maxima at 12 K are around 700 (band 3) and 850 nm (band 4). The infrared band around 1100 nm (band 5) is now strong in all crystals. The 600- and 800-nm bands completely vanish. The strong, sharp features around 650 nm in the gallium garnets are due to octahedral Mn^{4+} . Mn^{2+} with its typical emission around 590 nm is observed in YSGG, and very weakly in YAG. The assignment of these additional bands is possible by comparison with data from the literature.^{11,26–28}

In Fig. 7, the temperature dependence of the emission spectra is shown for Mn^{3+} :YAG. It is clearly observed that there is a continuous change of the intensities of the different bands from low temperature to room temperature. The temperature dependencies of the emission intensities are shown in Fig. 8; they were measured around 620 nm at the peak of the room-temperature short wavelength emission (band 1), and around 1120 nm at the peak of the infrared emission (band 5). The intensity of the visible emission band is first increasing with temperature and then decreasing (the falling edge of

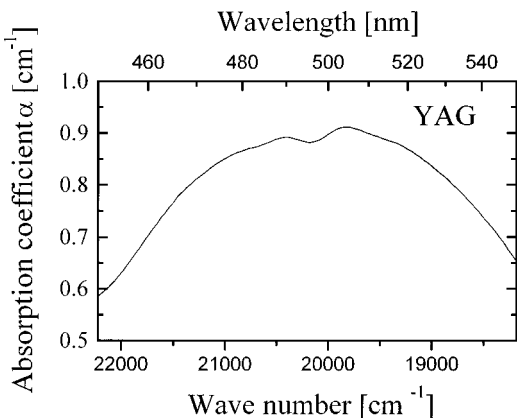


FIG. 4. Enlarged short wavelength part of the room-temperature absorption spectrum of Mn:YAG showing the Fano antiresonance at 500 nm.

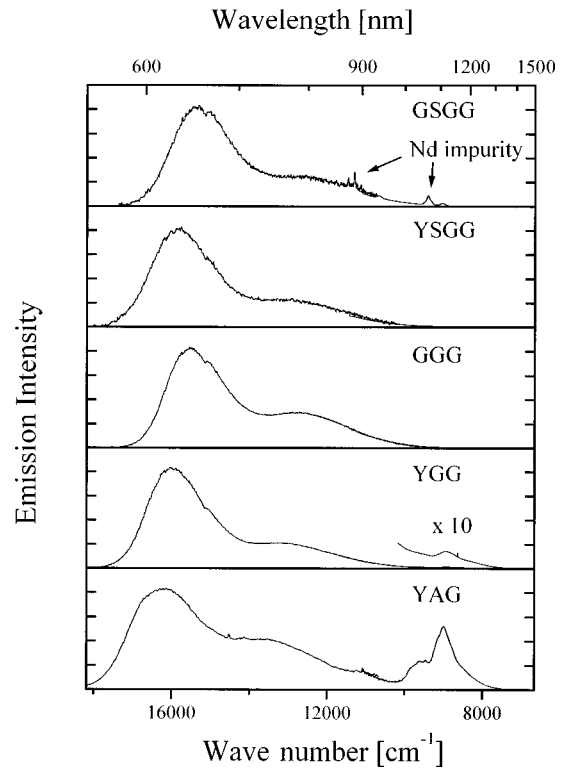


FIG. 5. Room-temperature emission spectra of Mn^{3+} -doped garnets. The sharp features in GSGG are due to a Nd^{3+} contamination.

Mn :YAG was not measured). The intensity of the infrared emission band is highest for low temperatures and then starts to decrease. This behavior of the emission spectra and of the intensities is caused by the thermalization of different electronic levels and nonradiative decay processes, as will be discussed in detail in the following sections.

The temperature dependencies of the Mn^{3+} lifetimes are shown in Fig. 9; the data at 12 K and room temperature are listed in Table VII. The decay times do not depend on the detection wavelength. The decay of all transitions is not purely single exponential in all crystals, most probably due to the coexistence of Mn ions in different valence states and possible energy transfer processes between these ions.

The $(I_p - I_u)/I_p$ spectra [see Eq. (1)] of Mn^{3+} are shown in Fig. 10. Note that a negative signal means dominating excited-state absorption, and a positive signal means dominating ground state absorption bleaching and/or stimulated emission.

V. DISCUSSION

In this section a model for the description of the observed spectroscopical properties of the Mn^{3+} ions is presented. This model is based on a strong Jahn-Teller distortion of the 5E ground state and weak distortions of the 5T_2 , 1E , 1T_2 , and 3T_1 excited states, resulting from the coupling of ϵ_g modes. In the following, a brief justification for this assumption is given.

The Jahn-Teller effect states, that an orbital degenerated electronic level of a many atomic, nonlinear molecule is unstable against a distortion, which lifts this degeneracy.¹ For a complex center with ideal octahedral symmetry O_h the coupling of an ϵ_g mode yields a splitting of the E , T_1 , and T_2

TABLE IV. Data of the room-temperature emission (bands 1 and 2). Abbreviations see caption of Table III. Index 1 (2) indicates transition ${}^5T_2 \rightarrow {}^5E'$ (${}^5T_2 \rightarrow {}^5E''$). $\Delta E({}^5T_2) = E_1 - E_2$. $\Delta E_{JT}({}^5T_2)$ is the Jahn-Teller stabilization energy of the 5T_2 level.

Crystal		GSGG	GGG	YSGG	YGG	YAG
λ_1	(nm)	659	654	641	631	620
E_1	(cm ⁻¹)	15 167	15 286	15 601	15 852	16 143
Γ_1	(cm ⁻¹)	1427	1441	1569	1312	1327
λ_2	(nm)	842	826	816	781	758
E_2	(cm ⁻¹)	11 884	12 104	12 254	12 803	13 199
Γ_2	(cm ⁻¹)	3391	2745	2936	3515	3799
$\Delta E({}^5T_2)$	(cm ⁻¹)	3283	3182	3347	3049	2944
Γ_2/Γ_1 , theor		2.61	2.55	2.42	2.36	2.38
Γ_2/Γ_1 , expt.		2.38	1.90	1.87	2.68	2.86
σ_1	(10 ⁻²⁰ cm ²)	5.4	4.7	6.7	3.4	3.7
σ_2	(10 ⁻²⁰ cm ²)	4.1	2.9	5.8	2.4	4.1
σ_1/σ_2		1.31	1.64	1.16	1.43	0.91
$\sigma_{1,\text{eff}}$	(10 ⁻²¹ cm ²)	25.6	4.1	2.9	1.1	0.4
$\Delta E_{JT}({}^5T_2)$	(cm ⁻¹)	366	347	348	308	301

levels, while the coupling of a τ_{2g} mode yields a splitting of the T_1 and T_2 levels only. According to their orbital degeneracy, the E level splits into two components and the T_1 and T_2 levels split into three components. For ε_g modes the vibrational distortions yield a change in the metal ion-ligand distance, while for τ_{2g} modes the ligand-metal ion-ligand angles are affected, leaving the distances unchanged. As a result, an ε_g distortion leads to a much larger Jahn-Teller stabilization energy than the τ_{2g} distortion.²⁹ Therefore, the

coupling of the τ_{2g} modes will be neglected in the further discussion, and only the coupling of ε_g modes to the E , T_1 , and T_2 levels will be considered. Furthermore, the effect of ε_g mode coupling is strongest for terms with configurations containing an unpaired, antibinding e_g electron. It will be weak for terms containing paired, antibinding e_g electrons and not binding t_{2g} electrons only.^{29,30} The configurations of the lowest-energy terms of the Mn³⁺ ion are

$${}^5E({}^5D):t_{2g}^3e_g,$$

$${}^5T_2({}^5D):t_{2g}^2e_g^2,$$

$${}^3T_1({}^3H):t_{2g}^4,$$

$${}^1T_2({}^1I):t_{2g}^4,$$

$${}^1E({}^1I):t_{2g}^4.$$

Only the 5E level has a configuration with one unpaired e_g electron. Thus the Jahn-Teller stabilization energy is expected to be highest, while for the other levels smaller stabilization energies are expected.

Before beginning with the detailed discussion of the spectroscopic results, it is reasonable to illustrate the model used for their description, and to make a few general predictions arising from this model. In Fig. 11, a schematic illustration of the effect of the ε_g mode coupling to the 5E and 5T_2 energy levels is shown. For the 5E ground state, the potential surface consists of a rotated parabola around the energy axis, the so-called ‘‘Mexican hat.’’²⁹ For the 5T_2 excited state the potential surface consists of three distinct paraboloids, i.e., it has no rotational symmetry;²⁹ see also Fig. 11. Here ε_v and ε_u are the two normal modes of the degenerated ε_g mode, and $q(\varepsilon_v)$ and $q(\varepsilon_u)$ are the corresponding coordinates, which transform like ε_v and ε_u . Because of the rotational symmetry of the ground-state potential surface, it is sufficient to look at a cut along the $q(\varepsilon_u)$ axis, that is along one of the axes, where one of the minima of the excited state

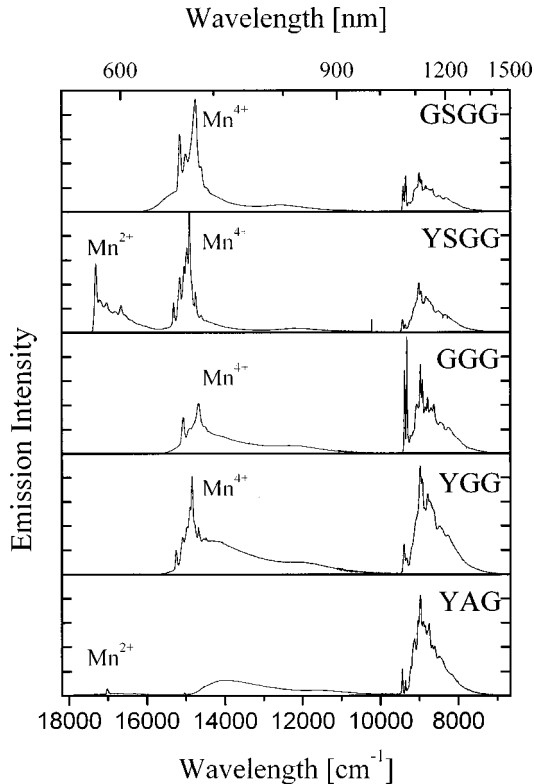


FIG. 6. 12-K emission spectra of Mn³⁺-doped garnets. The sharp features around 590 and 650 nm are caused by Mn²⁺ and Mn⁴⁺ ions, respectively.

TABLE V. Data of the 12-K emission (bands 3 and 4). Abbreviations see caption of Table III. Index 3 (4) indicates transition ${}^1T_2 \rightarrow {}^5E''$ (${}^1T_2 \rightarrow {}^5E'$); $\Delta E({}^1T_2) = E_3 - E_4$; $\Delta E_{JT}({}^1T_2)$ is the Jahn-Teller stabilization energy of the 1T_2 level.

Crystal		GSGG	YSGG	GGG	YGG	YAG
λ_3	(nm)	677	701	701	709	729
E_3	(cm^{-1})	14 780	14 630	14 262	14 112	13 712
Γ_3	(cm^{-1})	1060	1600	1144	1305	1600
λ_4	(nm)	801	832	828	843	879
E_4	(cm^{-1})	12 490	12 025	12 085	11 865	11 382
Γ_4	(cm^{-1})	2250	2600	2120	2270	2440
$\Delta E({}^1T_2)$	(cm^{-1})	2290	2605	2177	2247	2330
σ_4/σ_3		0.54	0.79	0.88	0.81	0.93
Γ_4/Γ_3 , theor.		1.91	1.96	1.85	1.85	1.96
Γ_4/Γ_3 , expt.		2.12	1.63	1.85	1.74	1.53
$\Delta E_{JT}({}^1T_2)$	(cm^{-1})	178	210	163	167	189

paraboloids are located. In Fig. 12 the resulting single-configurational coordinate model is shown schematically. Looking at the wave functions of the 5T_2 , 3T_1 , and 1T_2 levels, it can be shown,³¹ that the paraboloids of the 3T_1 , and 1T_2 levels are rotated by 60° with respect to the 5T_2 paraboloids. Therefore the absolute minima are at negative $q(\varepsilon_u)$ values. In Fig. 12, the 1E level is omitted for simplicity, because it is located approximately 1000 cm^{-1} above the 1T_2 level and has not to be taken into account in all further considerations.³² Under the assumption of equal force constants, the energetic position of the levels are described as follows [here, $q = q(\varepsilon_u)$ is used for simplicity]:

$$\begin{aligned}
 E({}^5E') &= c(q - q_0)^2, \\
 E({}^5E'') &= c(q + q_0)^2, \\
 E({}^3T_1) &= c(q + q_3)^2 + E_{30}, \\
 E({}^5T_2) &= c(q - q_5)^2 + E_{50}, \\
 E({}^1T_2) &= c(q + q_1)^2 + E_{10},
 \end{aligned} \tag{2}$$

where q_0 , $-q_0$, $-q_3$, q_5 , and $-q_1$ are the coordinates of the energetic minima of the ${}^5E'$, ${}^5E''$, 3T_1 , 5T_2 , and 1T_2 levels, respectively, E_{30} , E_{50} , and E_{10} are the energetic minima of the paraboloids, and c is a constant.

TABLE VI. Data of the 12-K infrared emission (band 5). $E_{ZPL,1}$ ($E_{ZPL,2}$) and $\Gamma_{ZPL,1}$ ($\Gamma_{ZPL,2}$) are the energetic position and bandwidth of zero phonon line (ZPL) 1 (2), respectively. $\Delta E_{ZPL,1,ZPL,2}$ is the energetic distance between the zero phonon lines, and σ_5/σ_3 is the ratio between the emission cross sections of transitions 5 and 3.

Crystal		GSGG	YSGG	GGG	YGG	YAG
$E_{ZPL,1}$	(cm^{-1})	9410	9432	9380	9396	9440
$\Gamma_{ZPL,1}$	(cm^{-1})	33	35	23	41	23
$E_{ZPL,2}$	(cm^{-1})	9347	9362	9322	9324	9363
$\Gamma_{ZPL,2}$	(cm^{-1})	34	47	24	61	21
$\Delta E_{ZPL,1,ZPL,2}$	(cm^{-1})	63	70	58	72	77
σ_5/σ_3		65	96	67	52	67

The ${}^5E \rightarrow {}^5T_2$ absorption is expected to be very broad, because the 5E potential surface has a rotational symmetry in the $[q(\varepsilon_v), q(\varepsilon_u)]$ plane. Therefore a large number of final states in the Jahn-Teller split 5T_2 level (three paraboloids) exists.

The energy E_{IR} of the ${}^5E' \rightarrow {}^5E''$ absorption band maximum is given by:

$$E_{IR} = E({}^5E'', q = q_0) = 4cq_0^2. \tag{3}$$

The bandwidth of this transition is proportional to the slope of the ${}^5E''$ level at $q = q_0$,

$$\Gamma_{IR} \propto \left. \frac{dE({}^5E'')}{dq} \right|_{q=q_0} = 4cq_0, \tag{4}$$

and therefore the relation between the bandwidth and the maximum is given by

$$\frac{\Gamma_{IR}}{\sqrt{E_{IR}}} = \text{const.} \tag{5}$$

The emission bands from the 5T_2 and 1T_1 levels arise from the local minima of the energy paraboloids. Therefore two emission bands from each level to the two Jahn-Teller-split

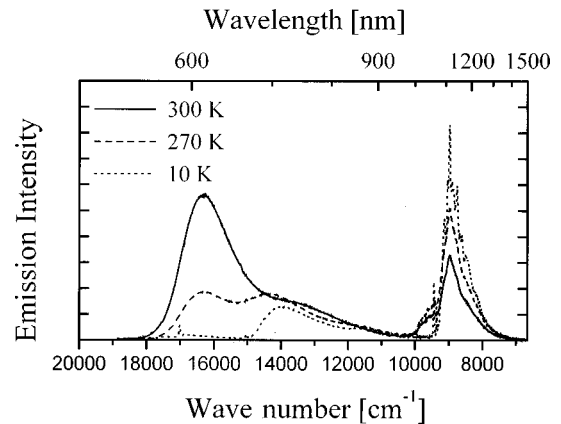


FIG. 7. Temperature dependence of the $\text{Mn}^{3+}:\text{YAG}$ emission.

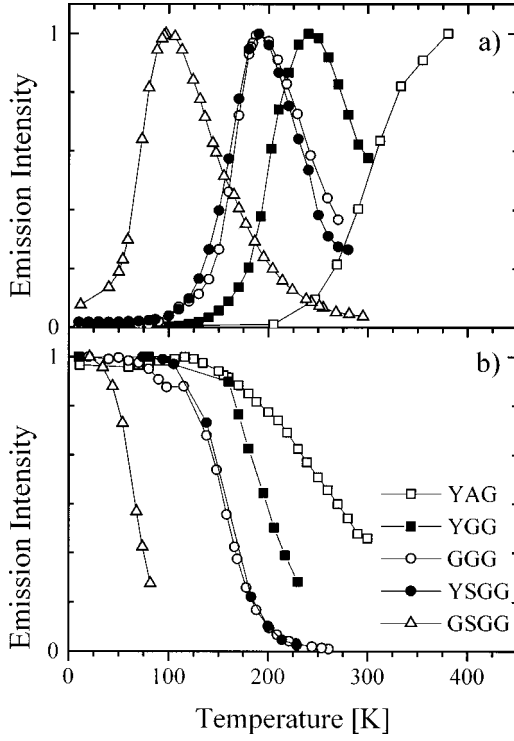


FIG. 8. Temperature dependence of the emission intensities. (a) band 1 (≈ 625 nm, ${}^5T_2 \rightarrow {}^5E'$); (b) band 5 (≈ 1100 nm, ${}^1T_2 \rightarrow {}^3T_1$).

components of the 5E ground state are expected. The energetic differences of the emission peaks of these two bands are expected to be

$$\Delta E({}^5T_2) = E({}^5E'', q=q_5) - E({}^5E', q=q_5) = 4cq_5q_0, \quad (6)$$

$$\Delta E({}^1T_2) = E({}^5E', q=-q_1) - E({}^5E'', q=-q_1) = 4cq_1q_0.$$

The bandwidth ratio Γ_2/Γ_1 of the emissions from the 5T_2 level to the 5E ground state are proportional to the ratio of the slopes of the 5E parabolas at q_5 , and the bandwidth ratio Γ_4/Γ_3 of the emissions from the 1T_2 level to the 5E ground state are proportional to the ratio of the slopes of the 5E parabolas at $-q_1$. Therefore, using Eqs. (2) and (6), the bandwidth ratios are

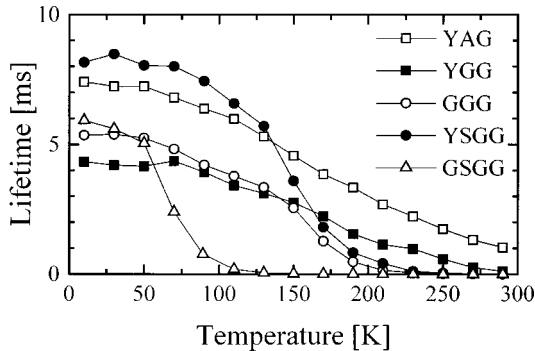


FIG. 9. Temperature dependence of Mn³⁺ lifetimes.

TABLE VII. Decay times at 12 K and at room temperature for the visible and infrared emission bands.

Crystal		GSGG	YSGG	GGG	YGG	YAG
τ (12 K)	(μ s)	5930	8150	5350	4330	7400
τ (300 K)	(μ s)	<0.5	4.7	2.7	104.4	1110

$$\frac{\Gamma_2}{\Gamma_1} \propto \left. \frac{\frac{dE({}^5E'')}{dq}}{\frac{dE({}^5E')}{dq}} \right|_{q=q_5} = \frac{|(q_5+q_0)|}{|(q_5-q_0)|} = \frac{|[E_{\text{IR}} + \Delta E({}^5T_2)]|}{|[E_{\text{IR}} - \Delta E({}^5T_2)]|},$$

$$\frac{\Gamma_4}{\Gamma_3} \propto \left. \frac{\frac{dE({}^5E')}{dq}}{\frac{dE({}^5E'')}{dq}} \right|_{q=-q_1} = \frac{|(-q_1-q_0)|}{|(-q_1+q_0)|} = \frac{|[E_{\text{IR}} + \Delta E({}^1T_2)]|}{|[E_{\text{IR}} - \Delta E({}^1T_2)]|}. \quad (7)$$

Finally, the Jahn-Teller stabilization energies can be calculated:

$$\Delta E_{JT}({}^5E) = E({}^5E', q=0) - E({}^5E'', q=0) = cq_0^2 = \frac{E_{\text{IR}}}{4},$$

$$\Delta E_{JT}({}^5T_2) = E({}^5T_2, q=0) - E({}^5T_2, q=q_5) = cq_5^2$$

$$= \frac{\Delta E({}^5T_2)^2}{c(4q_0)^2} = \frac{\Delta E({}^5T_2)^2}{4E_{\text{IR}}},$$

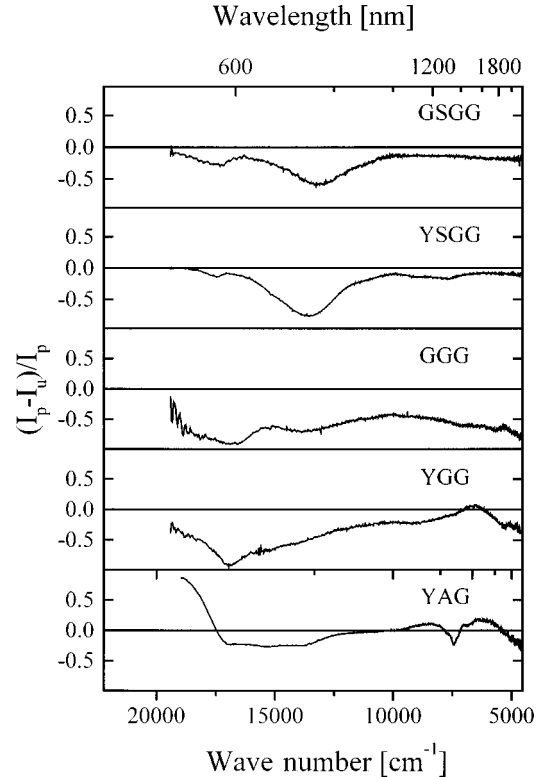


FIG. 10. Room-temperature $(I_p - I_u)/I_p$ spectra of Mn³⁺-doped garnets.

$$\begin{aligned}\Delta E_{JT}(^1T_2) &= E(^1T_2, q=0) - E(^1T_2, q=q_1) = cq_1^2 \\ &= \frac{\Delta E(^1T_2)^2}{c(4q_0)^2} = \frac{\Delta E(^1T_2)^2}{4E_{IR}}.\end{aligned}\quad (8)$$

A. Absorption

The dominating band around 500 nm in the absorption spectra—see Fig. 2—is assigned to the interconfigurational transition between the two Jahn-Teller-split quintet levels, i.e., the 5E ground state and the 5T_2 excited state. The large bandwidth of $\approx 4000\text{ cm}^{-1}$ for all investigated crystals is caused by the Jahn-Teller splitting of both energy levels. Large bandwidths are typical for transitions between Jahn-Teller split levels; see, for example, the $^2E \rightarrow ^2T_2$ emission in $\text{Ti}^{3+}:\text{Al}_2\text{O}_3$ and $\text{Ti}^{3+}:\text{YAG}$ with bandwidths of 3170 and 3425 cm^{-1} , respectively.³³ The absorption band shifts to shorter wavelengths with increasing crystal-field strength, as it is expected from the Tanabe-Sugano diagram; see Fig. 1. Note that the crystal-field strength is not proportional to the lattice constant. However, YAG is the crystal with the largest, and GSGG the crystal with the smallest, crystal-field strength. The energetic position of the feature on the short wavelength side of this main absorption band—see Fig. 4—is independent of the host crystal, i.e., the crystal-field strength. It is assigned to a Fano-antiresonance effect³⁴ between the 3E and 5T_2 levels. This antiresonance effect is based on the mixing between spin-orbit components of these levels. It is strong near the crossing of a spin-forbidden, crystal-field-independent term with a spin-allowed, crystal-field-dependent term.³⁵ With this antiresonance, it is possible to estimate the ratio between the crystal field strength Dq and the Racah parameter B . It is found for the garnets: $Dq/B \approx 2.3$.

The infrared-absorption band is assigned to a transition between the two Jahn-Teller-split components of the 5E ground state, as was observed for Mn^{3+} in acidic and aqueous solutions in Ref. 10. The large bandwidth of 3200–3900 cm^{-1} of this transition can be explained with a large Jahn-Teller energy, i.e., a large distortion. The shape of

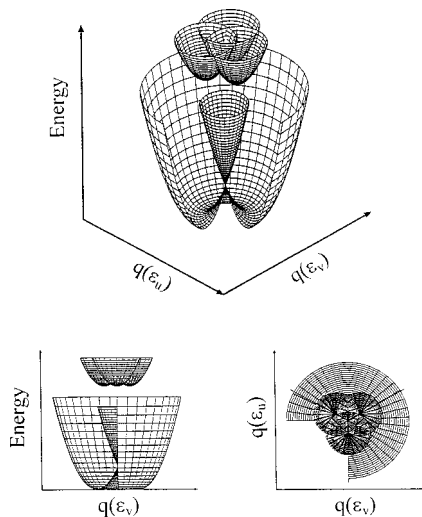


FIG. 11. Schematic illustration of ε_g mode coupling of the 5T_2 and 5E levels.

this band is nearly Gaussian, as is expected for a transition with a large Stokes shift. Here a clear relation between the crystal-field strength and the energetic position of this band is not found and also not expected, because the energetic difference between the two Jahn-Teller-split components of the 5E level is determined by the Jahn-Teller stabilization energy. This energy is not necessarily correlated to the crystal-field strength. The stabilization energies were calculated with Eq. (8), as listed in Table III. The values are between 1800 cm^{-1} for YAG and 2014 cm^{-1} for YSGG. In comparison, for $\text{Ti}^{3+}:\text{Al}_2\text{O}_3$ and $\text{Ti}^{3+}:\text{YAG}$ the Jahn-Teller stabilization energies of the 2E excited state were determined to 3081 and 2924 cm^{-1} , respectively;³³ for $\text{V}^{4+}:\text{Al}_2\text{O}_3$, $\Delta E_{JT}(^2E) = 2810\text{ cm}^{-1}$ was found.¹⁹ The ratio between the bandwidth Γ_{IR} and the square root of the energetic position of the absorption peak E_{IR} should be constant according to Eq. (4). As can be seen from Table III, these ratios are within reasonable margins. For all of these comparisons between calculated and experimental values it has to be taken into account that Eqs. (4) and (8) contain the peak absorption energy E_{IR} and the bandwidth Γ_{IR} of the infrared absorption. Both values have relatively high uncertainties, because the absorption is rather weak and extends beyond 2.5 μm which is the upper wavelength limit of the spectrophotometer.

In Table III, the ratios between the absorption coefficients in the visible and in the infrared are listed for the investigated crystals. As expected, they are roughly the same for all crystals, because both are spin-allowed transitions from the

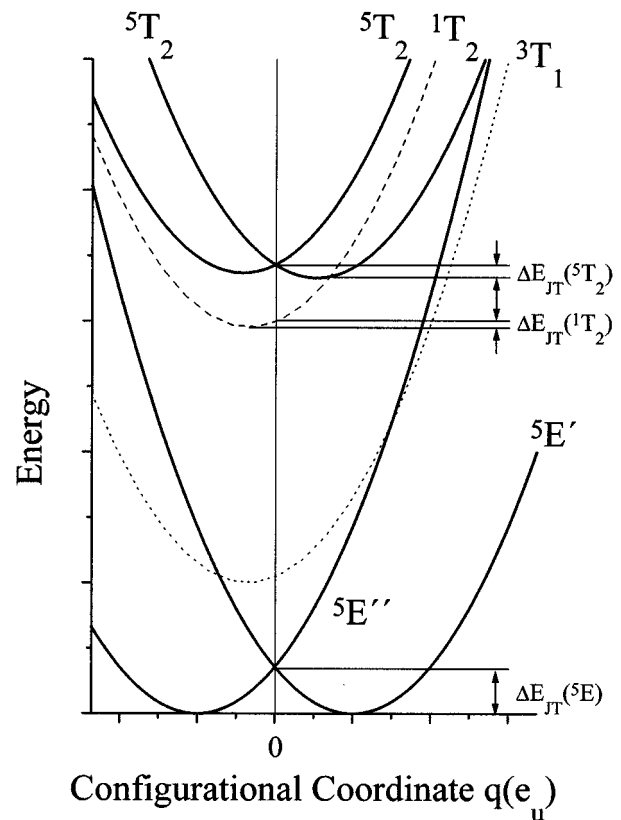


FIG. 12. Single-configurational coordinate model for ε_g mode coupling. For simplicity, only one Jahn-Teller component of the 1T_2 and 3T_1 levels is shown. The 1E level is omitted.

Mn^{3+} ground state. The absorption cross sections were determined from the absorption spectrum and the manganese concentration in the crystal. For YSGG the peak values are $4.5 \times 10^{-20} \text{ cm}^2$ (at 517 nm) and $0.74 \times 10^{-20} \text{ cm}^2$ (at 1433 nm). For YGG, they are $16.6 \times 10^{-20} \text{ cm}^2$ (at 512 nm) and $1.31 \times 10^{-20} \text{ cm}^2$ (at 1326 nm). These values have to be considered as lower limits, because only the total manganese concentration, i.e., Mn^{2+} , Mn^{3+} , and Mn^{4+} , was determined.

B. Room-temperature emission

The room-temperature emission consists of two bands in the visible spectral range with maxima around 630 and 800 nm. These bands dominate at elevated temperatures, because the emission from the 1T_2 level is spin forbidden. The 1T_2 emission can only be seen at low temperatures, when the population of the 5T_2 level is small (see Sec. V C). The bands at 630 and 800 nm are due to the transitions between the 5T_2 excited state and the two components of the Jahn-Teller-split 5E ground state. They exhibit a blueshift with increasing crystal-field strength as expected from the Tanabe-Sugano diagram and from the absorption spectra. The band shapes are Gaussian with bandwidths of about 1420 (${}^5T_2 \rightarrow {}^5E'$) and 3300 cm^{-1} (${}^5T_2 \rightarrow {}^5E''$). In comparison, for the ${}^2T_2 \rightarrow {}^2E$ absorption in $\text{Ti}^{3+}:\text{Al}_2\text{O}_3$ bandwidths of 1000 and 1300 cm^{-1} were determined.³³ The difference in the bandwidths for the Mn^{3+} emission is much larger because of the larger Jahn-Teller stabilization energy: For the Mn^{3+} -doped garnets, $\Delta E_{\text{JT}}({}^5T_2)$ is between 300 and 366 cm^{-1} [calculated with Eq. (8)] and therefore three times higher than $\Delta E_{\text{JT}}({}^2T_2) \approx 100 \text{ cm}^{-1}$ for $\text{Ti}^{3+}:\text{Al}_2\text{O}_3$.³³

The ratio between the bandwidths was also calculated from the energetic difference between the two emission maxima $\Delta E({}^5T_2)$ and the peak of the infrared absorption [see Eq. (7)] and compared with the experimentally determined ratios. The results are listed in Table IV. For YAG, YGG, and GSGG, the agreement is satisfactory, while for YSGG and GGG the deviations are rather large. However, here again it has to be considered, that Eq. (7) contains the energetic position of the infrared-absorption peak, which has large error bars. Furthermore, the short wavelength part of the emission in $\text{Mn}^{3+}:\text{YSGG}$ is overlapped by Mn^{2+} and/or Mn^{4+} emission (see Fig. 5), which could yield an overestimation of Γ_1 .

C. Low-temperature emission

The low-temperature emission spectra of the Mn^{3+} ion consists of transitions from the 1T_2 energy level. The 5T_2 level is not populated at these temperatures, and therefore no emission from this level is observed. The energetic distance between the 1T_2 and 5T_2 will be determined later from spectroscopic data and from the temperature dependence of the lifetime. The double-structured band with maxima around 700 and 850 nm (see Fig. 6) is caused by transitions into the Jahn-Teller-split components of the 5E ground state. In contrast to the room-temperature emission spectra, these low-temperature bands exhibit a redshift with increasing crystal-field strength. This can easily be explained by inspection of the Tanabe-Sugano diagram (Fig. 1). The 1T_2 level has an

inverse crystal-field dependence in comparison to the 5T_2 level, i.e., with increasing crystal-field strength the energetic position of the 1T_2 level is decreased with respect to the 5E ground state. As in Sec. IV B the experimentally determined bandwidth ratio can also be compared with the calculated one using Eq. (7). As can be seen in Table V, the agreement is satisfactory for all crystals. Larger deviations only appear for YAG and YSGG. The reason for the large deviations there is not yet clear.

D. Infrared emission

The third strong band in the low-temperature emission spectra is in the infrared spectral region around 1150 nm . This band is assigned to the transition between the 1T_2 and 3T_1 levels. As expected from the Tanabe-Sugano diagram (Fig. 1), the energetic position of this band is nearly independent of the crystal-field strength, i.e., the host crystal, because both levels have the same crystal-field dependence. Furthermore, they exhibit a smaller bandwidth and a distinctive phonon sideband structure. In all investigated systems, two zero-phonon lines are clearly observed with an energetic distance of about 70 cm^{-1} . The intensity ratio of these two lines is temperature independent. Therefore a splitting of the energetically higher 1T_2 is excluded. Two different emitting centers are also rather unlikely, because in the garnet structure different centers are not expected, especially not in YAG and YGG. Therefore, a splitting of the 3T_1 level is very likely. It is not clear whether spin-orbit coupling or lowering of the crystal-field symmetry accounts for the observed splitting. The Ham effect,³⁶ i.e., the reduction of the spin-orbit splitting because of a Jahn-Teller distortion, should play an inferior role in this case of small Jahn-Teller energies, so that a spin-orbit splitting of 70 cm^{-1} is a reasonable value. On the other hand, a crystal-field splitting into two energy levels is expected for a symmetry reduction from O_h to C_{3i} . Since the observed Jahn-Teller splitting is small, this static crystal-field symmetry reduction should also be taken into account. The phonon sideband structure is nearly identical for all investigated crystals; see Fig. 6. Therefore, the coupling phonons are assigned to modes of the $(\text{MnO}_6)^{9-}$ complex. However, a more detailed analysis of the sideband structure and the symmetry of the coupling phonons is beyond the scope of this paper, and will not be given here.

E. Temperature dependence of the emission

The temperature-dependent emission spectra of the Mn^{3+} -doped garnets, shown in Fig. 7 for $\text{Mn}^{3+}:\text{YAG}$, are in perfect agreement with the above-developed model. At 12 K , only the 1T_2 level is occupied, and the emission consists of three bands, as described in the Secs. V C and V D. As the temperature is increased, the 5T_2 level is thermally populated, so that at 250 K the quintet emission bands around 620 and 780 nm appear. At room temperature, the spectra are dominated by these emission bands only. The temperature of the emission onset depends on the energetic difference between the 1T_2 and 5T_2 levels, i.e., on the crystal-field strength and consequently on the host crystal. This can be seen in Fig. 8, where the intensity of the 620-nm emission band is shown as a function of temperature. The intensity rises up to a host specific temperature. Afterwards it de-

increases again, because then strong nonradiative decay processes dominate, as will be discussed in Sec. V F. The infrared emission intensity, on the other hand, remains constant for low temperatures. At higher temperatures the intensity drops due to a smaller population in this level. Further increase of the temperature yields a drastic intensity decrease due to strong nonradiative decay processes. In GSGG, YSGG, and GGG, the intensity of this infrared emission band finally drops below the detection limit of the detector.

F. Temperature dependence of the lifetime

The emission lifetimes of the Mn^{3+} -doped garnets are strongly dependent on the temperature, and at higher temperatures also on the host lattice. At low temperatures, the decay times are a few milliseconds for all investigated crystals, while at room temperature the lifetimes decrease and are between 1.1 ms for Mn:YAG and $<0.5 \mu\text{s}$ for Mn:GGG, see Table VII. In general, for the description of the temperature dependence of emission lifetimes, temperature-dependent radiative and nonradiative rates have to be considered. In the case of the Mn^{3+} ion; the thermal coupling between the different excited levels plays also an important role. The radiative rate increases drastically due to the population of the 5T_2 level, which enables the spin-allowed transition into the 5E ground states; see Secs. V B and V C. Thus

$$W_{r,0}(T) = \frac{3W_s + 15W_q \exp\left(-\frac{\Delta E}{kT}\right)}{3 + 15 \exp\left(-\frac{\Delta E}{kT}\right)}, \quad (9)$$

where $W_{r,0}(T)$ is the total static radiative rate, and W_s and W_q are the static radiative rates from the 1T_2 and 5T_2 , respectively, ΔE is the energetic distance between 1T_2 and 5T_2 , 3 and 15 are the degeneracies of the two levels, and $3 + 15 \exp(-\Delta E/kT)$ is the partition function.

In a crystal field with inversion symmetry, the $3d$ inner-shell transitions are magnetic dipole allowed only. However, coupling of odd-parity phonons to these transitions induces vibronically electric-dipole transition probability. This is taken into account with a coth factor for the temperature dependence of the radiative rate:¹²

$$W_r(T) = W_{r,0}(T) \coth\left(\frac{E_{\text{vib}}}{2kT}\right) = \frac{\left\{3W_s + 15W_q \exp\left(-\frac{\Delta E}{kT}\right)\right\} \coth\left(\frac{E_{\text{vib}}}{2kT}\right)}{3 + 15 \exp\left(-\frac{\Delta E}{kT}\right)}, \quad (10)$$

where E_{vib} is the energy of the coupling odd-parity phonon. For simplification, a single effective phonon energy is assumed for the coupling to the involved energy levels.

The radiative transitions were described under the assumption of ε_g mode coupling. However, looking at the single configurational coordinate model for ε_g mode coupling, nonradiative decay processes are unlikely, because the energy gaps between the energy levels are rather high; see

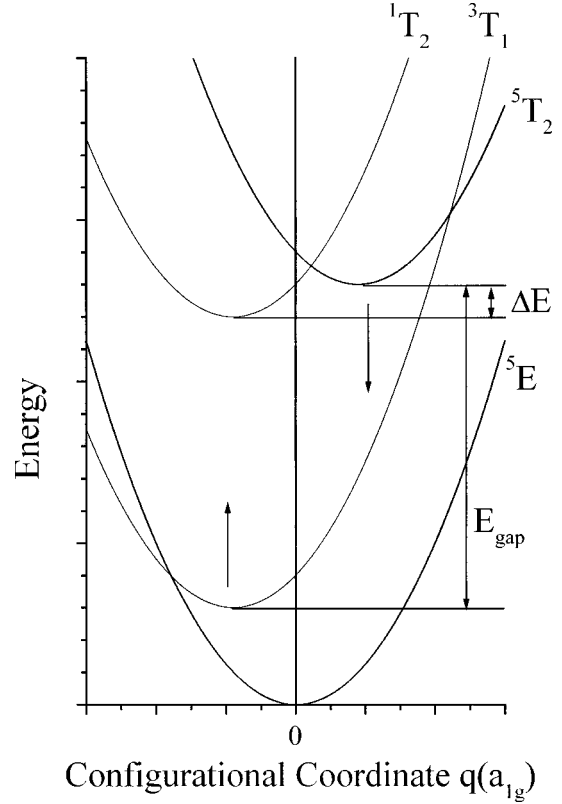


FIG. 13. Single-configurational coordinate model for α_{1g} mode coupling. The arrows indicate the shift of the 5T_2 and 3T_1 levels with decreasing crystal-field strength.

Fig. 12. So, for the description of the temperature-dependent nonradiative decay rates, a_{1g} mode coupling has to be considered. The single configurational coordinate model for this totally symmetric phonon coupling is shown in Fig. 13. Here a strong temperature-dependent quenching process between the 5T_2 and 3T_1 levels is possible. Since both levels have an inverse crystal-field dependence, this also explains the dramatic influence of the crystal-field strength on the observed emission intensities (see Fig. 8), and on the lifetimes. Because this quenching process occurs from the 5T_2 level, the thermal population has also to be taken into account, i.e., the energetic distance between the 1T_2 and 5T_2 levels. In the following, the temperature dependence of the nonradiative decay rate will be derived with the Struck-Fonger model.¹³ For simplification of the model, harmonic potentials and equal force constants in the ground and excited states are assumed. Within the Stirling approximation (valid for $p^* > 1$), the total nonradiative rate can then be expressed by³⁷⁻⁴⁰

$$W_{\text{nr}} = R_{\text{nr}} \exp(-S\langle 2m+1 \rangle) \frac{\exp(p^*)}{\sqrt{2\pi p^*}} \left(\frac{2S\langle 1+m \rangle}{p+p^*}\right)^p \times \frac{15 \exp\left(-\frac{\Delta E}{kT}\right)}{3 + 15 \exp\left(-\frac{\Delta E}{kT}\right)}, \quad (11)$$

with

TABLE VIII. Fit parameter describing the temperature-dependent decay rate. For explanations, see text.

Crystal		GSGG	YSGG	GGG	YGG	YAG
$1/\tau_{\text{rad},1}$	(1/s)	168	118	185	226	135
$1/\tau_{\text{rad},5}$	(1/s)	68 400	62 700	90 000	47 800	45 300
$h\omega_{\text{vib}}$	(cm ⁻¹)	155	155	155	155	155
ΔE	(cm ⁻¹)	351	900	900	1030	1290
$h\omega$	(cm ⁻¹)	306	306	306	306	
R_{nr}	(1/s)	10 ¹⁴	10 ¹⁴	10 ¹⁴	10 ¹⁴	
p		21	22	22	26	
S		4	4.12	4.12	4.84	
T_{nr}	(K)	90	130	160	230	300
η		<0.05	<0.05	<0.05	0.4	1
$\Delta E(^1T_2 - ^5T_2)$, (calculated from spectroscopic data)	(cm ⁻¹)	267	642	1124	1621	2348

$$p^* = \sqrt{p^2 + 4S^2\langle 1+m \rangle \langle m \rangle},$$

$$\langle m \rangle = \frac{r}{1-r} = \frac{1}{\exp\left(\frac{\hbar\omega}{kT}\right) - 1},$$

$$r = \exp\left(-\frac{\hbar\omega}{kT}\right),$$

where R_{nr} is the nonradiative decay constant ($\approx 10^{14}$ Hz), S is the Huang-Rhys parameter, p is the number of phonons bridging the energy gap E_{gap} between the 5T_2 and 3T_1 levels, $\hbar\omega$ is the energy of the effective phonon, and ΔE is the energetic distance between 1T_2 and 5T_2 .

Thus the total decay rate is given by:

$$\begin{aligned}
W(T) &= W_r(T) + W_{nr}(T) \\
&= \frac{\left\{ 3W_s + 15W_q \exp\left(-\frac{\Delta E}{kT}\right) \right\} \coth\left(\frac{E_{\text{vib}}}{2kT}\right)}{3 + 15 \exp\left(-\frac{\Delta E}{kT}\right)} \\
&\quad + R_{nr} \exp(-S\langle 2m+1 \rangle) \frac{\exp(p^*)}{\sqrt{2\pi p^*}} \left(\frac{2S\langle 1+m \rangle}{p+p^*}\right)^p \\
&\quad \times \frac{15 \exp\left(-\frac{\Delta E}{kT}\right)}{3 + 15 \exp\left(-\frac{\Delta E}{kT}\right)}. \tag{12}
\end{aligned}$$

The temperature dependence of the decay rate is therefore described with eight parameters, i.e., W_s , W_q , ΔE , E_{vib} , R_{nr} , S , p , and $\hbar\omega$. However, not all parameters are independent of each other, i.e., the relation between the energy gap and the number of phonons is $p\hbar\omega = E_{\text{gap}}$ (see Fig. 13). Furthermore, some parameters are set constant for all crystals, i.e., E_{vib} , $\hbar\omega$, and R_{nr} ($= 10^{14}$ Hz).¹³ Finally, it was assumed that the decay at 12 K is pure radiative, i.e., $\tau(12 \text{ K})^{-1} = W_s$. In general, all variations of the parameters should be small, because all host crystals are garnets. Only ΔE and p

depend significantly on the host crystal. After these considerations, the measured lifetimes and transitions rates were fit. The best fit was achieved with the parameters listed in Table VIII; the fit curves are shown in Fig. 14. The agreement between the calculated lifetimes (rates) with the experimentally determined ones are satisfactory. It is important to note, that the value of the parameters do not change very much between the crystals, i.e., the model seems to be consistent and valid to describe the situation in the Mn³⁺-doped materials. For comparison, the energetic distance ΔE between the 5T_2 and 1T_1 minima can also be calculated from the spectroscopic results using some geometrical consideration (see Fig. 12):

$$\begin{aligned}
\Delta E &= [E_{50} + \Delta E_{\text{JT}}(^5T_2)] - [E_{10} + \Delta E_{\text{JT}}(^1T_2)] \\
&= E_1 + E(^5E', q=q_5) + \Delta E_{\text{JT}}(^5T_2) - E_3 \\
&\quad - E(^5E'', q=-q_1) - \Delta E_{\text{JT}}(^1T_2) \\
&= E_1 - E_3 + 2[\Delta E_{\text{JT}}(^5T_2) - \Delta E_{\text{JT}}(^1T_2)] \\
&\quad + \frac{1}{2}[\Delta E(^1T_2) - \Delta E(^5T_2)]. \tag{13}
\end{aligned}$$

In Table VIII, both values for ΔE are listed. Although there is a considerable difference between these values, it should be noted, that both exhibit the expected correlation between the crystal field strength and activation energy ΔE . Furthermore, it has to be considered that in the Struck-Fonger model only one effective phonon is considered, and therefore only an effective activation energy is determined. For the evaluation of the laser potential of Mn³⁺-doped garnets, the quantum efficiency η is an important parameter. It is defined as

$$\eta = \frac{W_{\text{rad}}}{W}. \tag{14}$$

For low temperatures, the quantum efficiency is assumed to be unity for all investigated crystals. This is expected, because the energy gaps between the energy levels involved in the nonradiative decay processes are large, and at low temperatures only 1T_2 is populated. The quantum efficiency decreases with temperature because of an efficient quenching process between the 5T_2 level and the 3T_1 level. The quenching process starts at a host-specific temperature T_{nr} ,

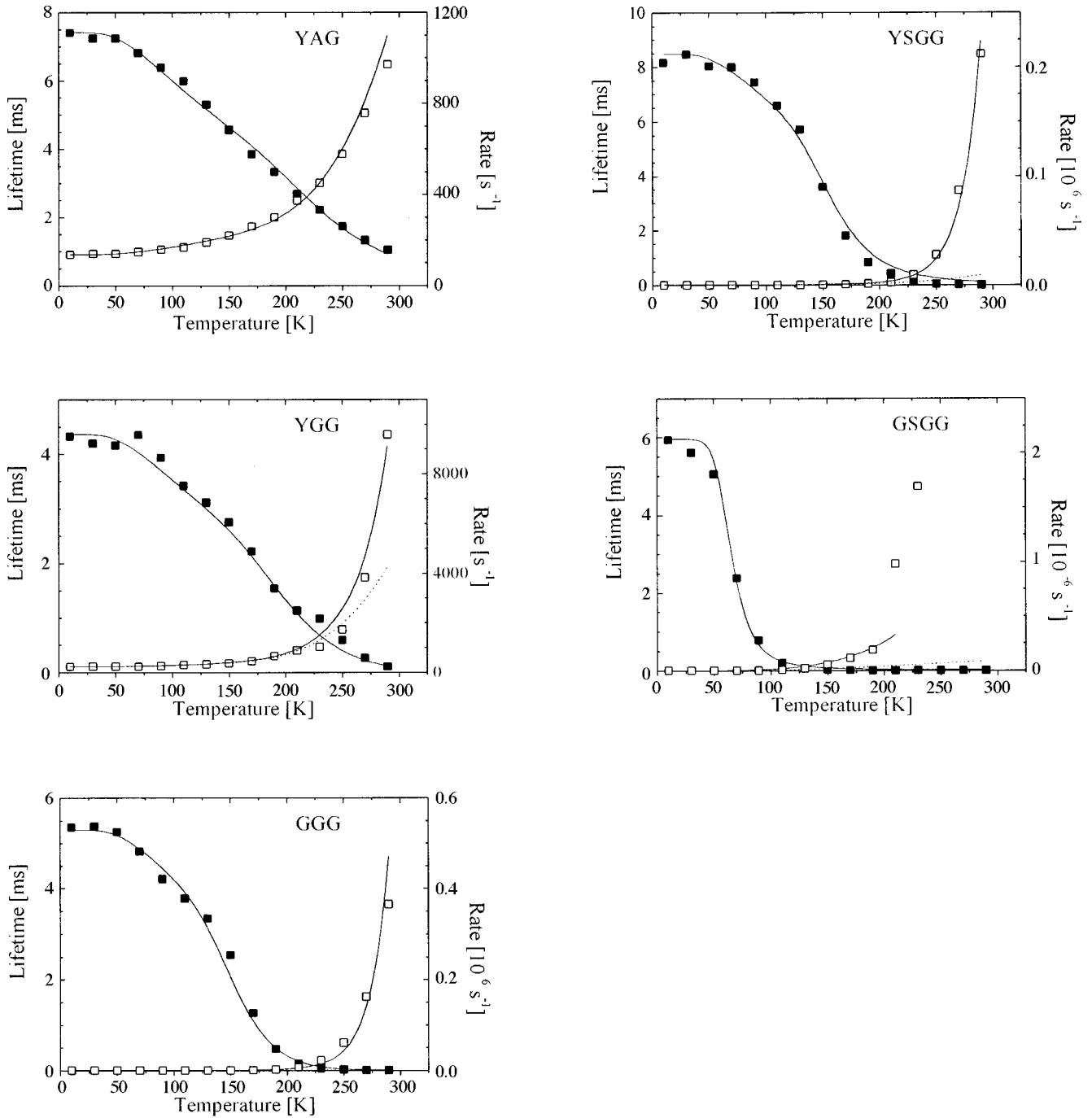


FIG. 14. Lifetimes and decay rates of Mn^{3+} -doped garnets. Solid lines are the fitted curves according to Eq. (12), and dashed lines are the radiative rates only. The parameters are listed in Table VIII.

which is between 90 K for GSGG and ≈ 300 K for YAG. At room temperature, the quantum efficiencies are near 1 for YAG, around 0.4 for YGG, and below 0.05 for YSGG, GSGG, and GGG, see Table VIII. As far as the quantum efficiency is concerned alone, efficient laser oscillation should only be achievable with Mn^{3+} :YAG and Mn^{3+} :YGG, while for GGG, YSGG, and GSGG the low value of the quantum efficiency yields an enormous increase in the threshold pump power. On the other hand, especially in YAG and YGG the 5T_2 level is only weakly populated because of the large ΔE . As a result, the effective cross sections are very small. In Fig. 15 the temperature dependence of the quantum efficiency is shown. This quenching behavior

with temperature and crystal-field strength is not unusual for transition metal ions in crystals. However, for Mn^{3+} -doped materials the effect of both temperature and crystal field strength is very pronounced. Looking at the Tanabe-Sugano diagram (Fig. 1), this quenching process is expected to occur. The energy gap between 5T_2 and 3T_1 decreases dramatically with decreasing crystal field, because of the inverse crystal-field behavior of both levels.

G. Emission cross sections

The emission cross section $\sigma_{\text{em}}(\nu)$ is proportional to the emission intensity $I_{\text{em}}(\nu)$. The absolute values for $\sigma_{\text{em}}(\nu)$ can be determined with help of the quantum efficiency⁴¹

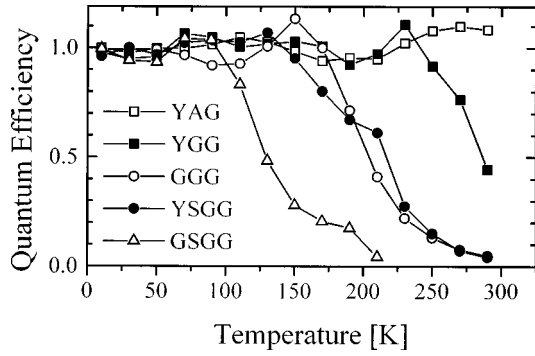


FIG. 15. Temperature dependence of the Mn^{3+} quantum efficiency.

$$\sigma_{\text{em}} = \beta \eta \left(\frac{c}{\nu n} \right)^2 \frac{I_{\text{em}}(\nu)}{8 \pi \tau \int I_{\text{em}}(\nu) d\nu}, \quad (15)$$

where β is the branching ratio, η the quantum efficiency, c the velocity of light, ν the frequency, n the refractive index, and τ the lifetime. For the room-temperature emission, i.e., the emission from the 5T_2 level, the branching ratio β is 0.5, because the relaxation takes place to the two components of the Jahn-Teller-split 5E ground state. The results for the bands 1 and 2 are listed in Table IV. The cross sections are of the order of $5 \times 10^{-20} \text{ cm}^2$, i.e., slightly higher than the ${}^4T_2 \rightarrow {}^4A_2$ emission cross sections for the Cr^{3+} ion in GSGG of about $1.1 \times 10^{-20} \text{ cm}^2$.⁴² However, like in the Cr^{3+} -doped garnets and Cr^{3+} -doped alexandrite, the effective emission cross sections at room temperature are the relevant values for the evaluation of Mn^{3+} -doped garnets as possible laser materials, that is the thermal population of the metastable 5T_2 level has to be considered. Thus

$$\sigma_{\text{em,eff}}(\lambda) = \sigma_{\text{em}}(\lambda) \frac{15 \exp\left(-\frac{\Delta E}{kT}\right)}{3 + 15 \exp\left(-\frac{\Delta E}{kT}\right)}, \quad (16)$$

where ΔE is the energetic difference between the 1T_2 and 5T_2 levels determined from the temperature dependence of the lifetime; see Eq. (12). These effective emission cross sections at room temperature are also given in Table IV. As expected, these values are lowest for YAG and YGG, because of the larger ΔE , which yields a small population of the 5T_2 level. In principle, the room-temperature emission cross section of the ${}^5T_2 \rightarrow {}^5E$ transition can also be determined from the reciprocity of the absorption and emission spectra. Thus

$$\sigma_{\text{em}}({}^5T_2 \rightarrow {}^5E) = \frac{2}{3} \sigma_{\text{abs}}({}^5E \rightarrow {}^5T_2), \quad (17)$$

where σ_{em} and σ_{abs} are the emission and absorption cross sections of the ${}^5E \leftrightarrow {}^5T_2$ transitions, respectively, and $\frac{2}{3}$ is the ratio of the degeneracies of the 5E and 5T_2 levels. For Mn^{3+} :YGG and Mn^{3+} :YSGG the emission cross sections are determined to be 11×10^{-20} and $3 \times 10^{-20} \text{ cm}^2$, respectively. They are in reasonable agreement with the values determined from Eq. (15), taking into account the uncertainty in the

determination of the absorption cross section and the quantum efficiency, see Secs. V A and V F.

At low temperatures, three emission bands are observed, i.e., ${}^1T_2 \rightarrow {}^5E'$, ${}^1T_2 \rightarrow {}^5E''$, and ${}^1T_2 \rightarrow {}^3T_1$. In general, the cross sections of these transitions are expected to be at least two orders of magnitude smaller than $\sigma_{\text{em}}({}^5T_2 \rightarrow {}^5E)$, because they are spin forbidden with $\Delta S = 2$ (${}^1T_2 \rightarrow {}^5E$) and $\Delta S = 1$ (${}^1T_2 \rightarrow {}^3T_1$). Therefore, here only the ratios between the cross sections will be given as determined by the Fuchtbauer-Ladenburg law:^{43,44}

$$\sigma_{\text{em}}(\lambda) \propto I(\lambda) \lambda^5, \quad (18)$$

where $I(\lambda)$ is the emission intensity. As expected from the comparison of $\Delta S = 1$ with $\Delta S = 2$, $\sigma_5/\sigma_3 \approx 50\text{--}100$, while σ_3 and σ_4 have the same order of magnitude; see Tables VI and V.

H. Excited-state absorption

The $(I_p - I_u)/I_p$ spectra of all Mn^{3+} -doped garnets reveal strong excited-state absorption within the whole visible emission range of the Mn^{3+} ion, see Fig. 10. Since only one excited quintet state 5T_2 with small Jahn-Teller splitting exists, no strong transitions arising from this level should be observed. The observed transitions are therefore assigned to transitions from the 1T_2 level into higher-lying singlet states. The Tanabe-Sugano diagram (Fig. 1) indicates a variety of singlet states. An exact assignment to specific transitions is not possible, because of the expected Jahn-Teller splitting of all these levels. Only the remarkable feature in the infrared spectral region around 1335 nm is most probably the transition to the 1A_1 (1G) level, because of its small bandwidth and energetic position. Ground-state absorption bleaching is observed for Mn^{3+} :YAG in the visible and in the infrared spectral range, according to the transitions ${}^5E \rightarrow {}^5T_2$ and ${}^5E \rightarrow {}^5E$. Stimulated emission is not observed in the spectra, i.e., it is totally covered by strong excited-state absorption processes. Therefore in the whole series of investigated Mn^{3+} -doped garnets crystals, laser oscillation at room temperature will not be possible.

VI. SUMMARY AND OUTLOOK

Mn^{3+} -doped garnet crystals were spectroscopically investigated in the visible and near-infrared spectral ranges. The observed spectroscopic characteristics can be explained with a strong Jahn-Teller splitting in the 5E ground state, and weaker Jahn-Teller splittings of the 5T_2 , 1T_2 , and 3T_1 excited states. The agreement between the theoretical predictions from ϵ_g -mode coupling and the measurements is satisfactory. Emissions occur from the 1T_2 level and the 5T_2 level into the energetically lower-lying 3T_1 and 5E levels. Thermalization of the 5T_2 and 1T_2 levels is clearly observed in the emission spectra and the temperature dependence of the emission intensity. The temperature dependence of the emission lifetimes can be described with satisfactory agreement with a model including the thermal activation of the 5T_2 level, the temperature dependent radiative rate—caused by odd-parity phonon coupling—and temperature-dependent nonradiative rates. The quantum efficiencies at room temperature are near unity for Mn:YAG, and below 0.05 for

Mn-doped GGG, YSGG, and GSGG. We emphasize that the observed optical spectra are based on the Jahn-Teller splitting of the energy levels according to an ϵ_g -mode coupling, while the nonradiative decay processes are dominated by a_{1g} mode coupling. Strong excited-state absorption due to singlet-singlet transitions overlaps the spectral regions of emission, therefore laser oscillation is not expected in these materials. To avoid excited-state absorption, a lower crystal field is necessary in order to have the 5T_2 level as lowest metastable level. In this case, the excited-state absorption is reduced, because from the 5T_2 only spin forbidden transitions to higher-lying levels occur. However, in this case the quantum efficiency is expected to be even less than for Mn:GSGG. As a consequence, low-phonon host lattices

should be preferred, e.g., fluorides, which would decrease the nonradiative decay processes. Another possible way would be the use of host lattices with strong polarization-dependent optical spectra, in order to achieve a high polarized quintet-quintet emission cross section with a simultaneously low excited state absorption cross section in this polarization and high quantum efficiencies. However, since the 5T_2 level will only be thermally populated in this case, only a small gain is expected.

ACKNOWLEDGMENT

The authors would like to thank Dr. Joachim Degen from the University of Düsseldorf for valuable discussions.

*FAX: 49 40 4123 6281. Electronic address: kueck@physnet.uni-hamburg.de

¹H. A. Jahn and E. Teller, Proc. R. Soc. London, Ser. A **161**, 220 (1937).

²H. D. Koswig and I. Kunze, Phys. Status Solidi **9**, 451 (1965).

³H. D. Koswig, U. Retter, and W. Ulrici, Phys. Status Solidi B **51**, 123 (1972).

⁴W. Ulrici, Phys. Status Solidi B **51**, 129 (1972).

⁵G. Goetz, H. Zimmermann, and H.-J. Schulz, Z. Phys. B **91**, 429 (1993).

⁶D. S. McClure, J. Chem. Phys. **36**, 2757 (1962).

⁷R. M. Macfarlane, J. Y. Wong, and M. D. Sturge, Phys. Rev. **166**, 250 (1968).

⁸M. Grinberg, A. Mandelis, F. Fjeldsted, and A. Othonos, Phys. Rev. B **48**, 5922 (1993).

⁹R. Dingle, Mol. Spectrosc. (Chem. Soc., London) **9**, 426 (1962).

¹⁰T. S. Davis, J. P. Fackler, and M. J. Weber, Inorg. Chem. **7**, 1994 (1968).

¹¹K. Petermann and G. Huber, J. Lumin. **31&32**, 71 (1984).

¹²B. Henderson and G. F. Imbusch (Clarendon, Oxford, 1984).

¹³C. W. Struck and W. H. Fonger, J. Lumin. **10**, 1 (1975).

¹⁴P. F. Moulton, Opt. News **8**, 9 (1982).

¹⁵P. F. Moulton, J. Opt. Soc. Am. B **3**, 125 (1986).

¹⁶P. Albers, E. Stark, and G. Huber, J. Opt. Soc. Am. B **3**, 134 (1986).

¹⁷R. Rao, G. Vaillancourt, H. S. Kwok, and C. P. Khattak, in *Tunable Solid State Lasers*, edited by M. L. Shand and H. P. Jensen, Vol. 5 of OSA Proceedings Series (Optical Society of America, Washington, D.C., 1989), pp. 39–41.

¹⁸T. Danger, K. Petermann, and G. Huber, Appl. Phys. A: Solids Surf. **57**, 309 (1993).

¹⁹J. P. Meyn, T. Danger, K. Petermann, and G. Huber, J. Lumin. **55**, 55 (1993).

²⁰Y. Tanabe and S. Sugano, J. Phys. Soc. Jpn. **9**, 753 (1954).

²¹L. D. deLoach, R. H. Page, G. D. Wilke, S. A. Payne, and W. F. Krupke, IEEE J. Quantum Electron. **32**, 885 (1996).

²²G. Menzer, Z. Kristallogr. **69**, 300 (1928).

²³A. A. Kaminskii, *Laser Crystals* (Springer, Berlin, 1981).

²⁴S. Zemon, G. Lambert, W. J. Miniscalco, R. W. Davies, B. T. Hall, R. C. Folweiler, T. Wei, L. J. Andrews, and M. P. Singh, in *Fiber Laser Sources and Amplifiers II*, edited by M. J. Digonnet [Proc. SPIE **1373**, 21 (1991)].

²⁵J. Koetke and G. Huber, Appl. Phys. B: Lasers Opt. **61**, 151 (1995).

²⁶L. A. Riseberg and M. J. Weber, Solid State Commun. **9**, 791 (1971).

²⁷A. Brenier, A. Suchocki, C. Pedrini, G. Boulon, and C. Madej, Phys. Rev. B **46**, 3219 (1992).

²⁸H. Teichmann, Master's thesis, University of Hamburg, Germany, 1984.

²⁹M. D. Sturge, *Solid State Physics* (Academic, New York, 1967), Vol. 20, pp. 92–211.

³⁰H. L. Schläfer and G. Gliemann, *Einführung in die Ligandenfeldtheorie* (Akademische Verlagsgesellschaft, Wiesbaden, 1980).

³¹J. Degen (private communication).

³²J. Bendix, Ligfield Program, Department of Chemistry, University of Copenhagen, Denmark.

³³P. Albers, Ph.D. thesis, University of Hamburg, Germany, 1985.

³⁴U. Fano, Phys. Rev. **124**, 1866 (1961).

³⁵M. D. Sturge, H. J. Guggenheim, Phys. Rev. B **2**, 2459 (1970).

³⁶F. S. Ham, Phys. Rev. A **138**, 1727 (1965).

³⁷H. V. Lauer and F. K. Fong, J. Chem. Phys. **60**, 274 (1974).

³⁸W. H. Fonger and C. W. Struck, J. Chem. Phys. **69**, 4171 (1978).

³⁹M. Yamaga, Y. Gao, F. Rasheed, K. P. O'Donnell, B. Henderson, and B. Cockayne, Appl. Phys. B: Photophys. Laser Chem. **51**, 329 (1990).

⁴⁰S. Kück, K. Petermann, U. Pohlmann, and G. Huber, Phys. Rev. B **51**, 17 323 (1995).

⁴¹D. E. McCumber, Phys. Rev. A **136**, 954 (1964).

⁴²B. Struve, G. Huber, V. V. Laptev, I. A. Shcherbakov, and E. V. Zharikov, Appl. Phys. B: Photophys. Laser Chem. **30**, 117 (1983).

⁴³A. C. G. Mitchell and M. W. Zemansky, *Resonance Radiation and Excited Atoms* (Cambridge University Press, Cambridge, 1934).

⁴⁴B. A. Lengyel, *Lasers* (Wiley-Interscience, New York, 1971).